effect on its two symbiotic fishes *A. perideraion* and *A. clarkii*.

One of the chemicals responsible for the *A. perideraion–R. kuekenthali* symbiosis, amphikuemin, is particularly active and elicits a swimming pattern mimicking that caused by a crude mucous extract from the anemone. The heterocyclic nitrogen of amphikuemin is made quaternary, which presumably increases affinity to the negatively charged lipid surface of receptor membranes; *N*-demethyl-L-amphikuemin (a synthetic intermediate) was totally devoid of activity. The activity of the synthetic quaternary salt 4′-demethyl-L-amphikuemin was greatly reduced to $2.0 \times 10^{-8} M$, thus indicating the very specific structural requirement. However, since the experiments were carried out with young fish in an assay vessel, it is not known whether the same set of compounds is responsible for leading the naïve juvenile fish to their host at the initial encounter in the sea. In contrast to the *A. perideraion–R. kuekenthali* pair, it appears that induction of the swimming movement in *A. ocellaris–S. kenti* depends on the synergistic action of multiple chemicals not yet identified. We have also shown that different species of anemone fish recognize the same anemone species by different chemicals. Thus a variety of chemicals differing in structural type, activity level, and function are involved in maintaining the species-specific association between the sea anemone and anemone fish.

REFERENCES AND NOTES

1. J. Verwey, *Treubia* **12**, 3 and 305 (1930).
2. R. N. Mariscal, thesis, University of California, Berkeley (1966); *Univ. Calif. Publ. Zool.* **91**, 1 (1970).
3. R. G. Allen, *The Anemonefishes* (T. F. H. Publications, Neptune City, NJ, ed. 2, 1975).
4. D. Davenport and K. S. Norris, *Biol. Bull. (Woods Hole, Mass.)* **115**, 397 (1958).
5. D. Schlichter, *Z. Tierpsychol.* **25**, 933 (1968).
6. R. N. Mariscal, *Experientia* **25**, 1114 (1969); *J. Exp. Mar. Biol. Ecol.* **4**, 134 (1970).
7. K. Miyagawa, thesis, Kyoto University (1983); ——— and T. Hidaka, *Proc. Jpn. Acad. Ser. B Phys. Biol. Sci.* **56**, 356 (1980).
8. D. S. Nordland and W. J. Lewis, *J. Chem. Ecol.* **2**, 211 (1976).
9. D. F. Dunn, *Trans. Am. Philos. Soc.* **71**, part 1 (1981).
10. NMR spectroscopy data for the amphikuemin, 360 MHz (Nicolet NT 360), in D_2O where *d* is doublet, Me is methyl, *t* is triplet, and *m* is multiplet: 2′-H 8.48, 5′-H 7.81 (*d*, 6.5), 6′-H 8.46 (*d*, 6.5), N^+-Me 4.28, 4′-Me 2.58, 10-H 3.12 (*t*, 7.5), 9-H 2.62 (*t*, 7.5), 6-H 3.16 (*t*, 7.0), 5-H 1.49 (*m*), 4-H 1.38 (*m*), 3-H 1.88 (*m*), and 2-H 3.83 ppm (*t*, 6).
11. R. Kazlauskas, P. T. Murphy, R. J. Quinn, R. J. Wells, *Tetrahedron Lett.* **1977**, 61 (1977) (first isolation).
12. A. A. Tymiak and K. L. Rinehart, Jr., *Tetrahedron* **41**, 1039 (1985).
13. R. K. Okuda, D. Klein, R. B. Kinnel, M. Li, P. J. Scheuer, *Pure Appl. Chem.* **54**, 1907 (1982).
14. The procedure is based on that described by P. Djura and D. J. Faulkner [*J. Org. Chem.* **45**, 735 (1980)].

15. We are grateful to S. Uchida (director) and Y. Kamei, Okinawa Expo Memorial Park Aquarium, for provision of space and for collection and rearing of assay animals; and also to Yaeyama Marine Park Research Station; to M. Irie for discussions; to T. Higa, University of the Ryukyus, for use of laboratory space; to T. Hidaka, Kyoto University, for discussions; and to T. Iwashita, H. Naoki, Y. Ohfune, K. Tachibana, and K. Yoshihara of this institute for discussions, suggestions, and spectroscopic measurements.

20 May 1986; accepted 11 August 1986

Radar Glory from Buried Craters on Icy Moons

VON R. ESHLEMAN

Three ice-covered moons of Jupiter, in comparison with rocky planets and Earth's moon, produce radar echoes of astounding strengths and bizarre polarizations. Scattering from buried craters can explain these and other anomalous properties of the echoes. The role of such craters is analogous to that of the water droplets that create the apparition known as "the glory," the optically bright region surrounding an observer's shadow on a cloud. Both situations involve the electromagnetic phenomenon of total internal reflection at a dielectric interface, operating in a geometry that strongly favors exact backscattering. Dim surface craters are transformed into bright glory holes by being buried under somewhat denser material, thereby increasing the intensity of their echoes by factors of hundreds. The dielectric interface thus formed at the crater walls nicely accounts for the unusual polarizations of the echoes.

SINCE THE FIRST OBSERVATIONS more than a decade ago, a major puzzle in planetary science has been the unexpected results of radar studies of Europa, Ganymede, and Callisto, large ice-clad moons of Jupiter. These radar echoes can exceed the strengths that would be obtained if the moons were perfectly reflecting spheres. This, plus the odd polarizations and weak angular dependence of the echoes, characterizes their profound differences from the relatively well-understood radar signatures of terrestrial planets and Earth's moon (*1*). A new model is developed here in which the anomalous characteristics of the icy-moon echoes can be attributed to inherent scattering properties of buried craters.

Four previous attempts at explaining the observations have been less satisfactory. Ostro and Pettengill (*2*) proposed scattering by surface craters, but this mechanism cannot easily explain the measured echo strengths. Goldstein and Green (*3*) invoked random subsurface scattering events to model the observations, but this also has difficulty in accounting for the strengths of the echoes. Hagfors *et al.* (*4*) suggested scattering from smooth-gradient centers of refraction; this can explain the strengths but does not produce a good match to the observed polarizations. Eshleman (*5*) demonstrated that a decoupling of two characteristic modes of propagation may be fundamental in producing the odd polarizations and suggested several ways that the refracting centers of Hagfors *et al.* could be modified to produce the decoupling. Although the echo properties (*1*) can all be matched in this way, there is no other compelling reason to believe that such centers exist.

One of the suggested modifications to the refraction model involved sharp radial gradients in refractivity. These discontinuities could cause trapping of the two characteristic propagation modes, analogous to the trapping that occurs in dielectric waveguides and optical fibers, thereby differentially shifting their phases and decoupling them as required. Moreover, Eshleman (*5*) noted that such a trap might provide the necessary backward focusing even in the absence of the smooth refraction proposed by Hagfors *et al.* (*4*). A particularly simple model of this type is introduced here. It consists of a single negative discontinuity of refractive index in a hemispheroidal geometry, or more descriptively, a buried crater. This model is appealing, since it is known that both cratering and resurfacing have occurred on the icy moons.

Perfect geometrical shapes cannot explain the observations (*5*) and are not expected to occur. Thus the craters are considered to be hemispheroidal with their imperfections causing a breakup of the coherent annulus of the glory circle (the locus of intersection of the backscattered rays and a plane normal to the incident rays at the crater) into discrete patches or glints. From an extension of a quasi-wave-optical analysis of spheroidal

Department of Electrical Engineering and Center for Radar Astronomy, Stanford University, Stanford, CA 94305.

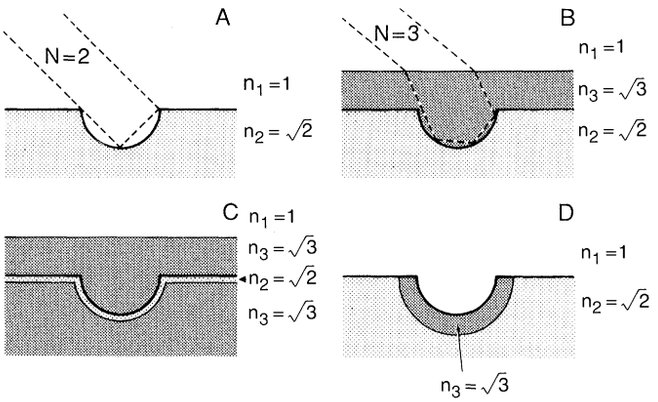

Fig. 1. Representative refractive indices and ray paths to illustrate backscattering from surface and buried craters: (A) surface crater with $n = n_1/n_2 = (0.5)^{1/2}$ and $N = 2$ ray bounces; (B) buried crater with $n = n_3/n_2 = (1.5)^{1/2}$ and $N = 3$; (C) buried crater with $n = (1.5)^{1/2}$ due to a thin layer caused by frost deposits or sublimation of ice; (D) crater wall compressed or lined to produce $n = (1.5)^{1/2}$ as for the buried craters.

centers of refraction (*5*), the radar backscatter cross sections of either surface or buried craters in lossless dielectrics can be obtained from

$$\frac{\sigma_N}{\pi r_0^2} = \left(\frac{FH}{\lambda}\right)\left(\frac{4\pi n_B}{N n_c^2}\right)\left(|\rho_{TM}|^{2N} + |\rho_{TE}|^{2N}\right)$$

with

$$\rho_{TM} = \frac{n(n_c^2 - n^2)^{1/2} - n_B}{n(n_c^2 - n^2)^{1/2} + n_B}$$

$$\rho_{TE} = \frac{nn_B - (n_c^2 - n^2)^{1/2}}{nn_B + (n_c^2 - n^2)^{1/2}}$$

Here, $N \geq 2$ is the number of crater-wall reflections; σ_N is the radar cross section for that N; r_0 is the crater radius; H is the circumferential dimension of a representative glint with the requirement that $r_0 > H > \lambda$, where λ is the radar wavelength; F is the fraction of the glory circle filled by the glints; n is the ratio of the refractive index at $r < r_0$ to that of the crater base at $r > r_0$; n_B is the corresponding ratio that would make the N–bounce path occur at the Brewster angle; n_c is the ratio for it to occur at the angle of total internal reflection; and the ρ values are the Fresnel reflection coefficients for the transverse magnetic (TM) and transverse electric (TE) modes, where the electric vector is in, or normal to, the plane of propagation, respectively (*6*).

Table 1 shows for comparison an example of the radar cross sections of a surface crater (Fig. 1A) and a buried crater (Fig. 1B) of the same size in material of the same refractive index. The overburden is assumed to have a higher index, which is representative of ice at normal density. The illustrated rays demonstrate that a cratered surface can exhibit the bright-limb aspect of the observations (*1*), and that the buried craters are better than surface craters in this regard. This important effect is not developed further in order to emphasize other features of the model.

The results in Table 1 are for $\sigma_N/\pi r_0^2$, the normalized radar backscatter cross sections, for various values of N. For $N \geq 2$, they include an assumption about the value of the common term (FH/λ), taken here to be 10 as would be obtained, for example, if $F = 0.5$, $H = 2$ m, and $\lambda = 0.1$ m. The maximum possible value of this term at this wavelength would be about 30 to 300 for crater radii between 1 and 10 m. This assumption is believed to be conservative and relatively independent of the sizes of the coherent zones over a limited range, since one would expect a larger (smaller) number of them if they were smaller (larger) in size. It is also assumed that the direction of incidence is such that none of the rays is intercepted by crater rims. For the buried crater, no correction is made for the small power loss due to the two traverses of the upper boundary. The important result in Table 1 is the enormous ratio of cross sections when $N \geq 3$. This is due to total internal reflection (TIR) in the buried crater when $n > n_c$. The sudden onset of TIR with increasing n is particularly evident in Fig. 2A, which shows the values of the radar cross sections.

The value of the backscatter cross section in Table 1 for the buried crater with $N = 3$ means that this single component of echo energy is 36 times the total echo that would be returned from a perfectly reflecting sphere of the same radius. For the strongest scatterer, Europa, $\sigma/\pi R^2 = 2.6$ where R is its radius. The $N = 3$ component alone could yield this value if only 7% of the surface area were covered with buried craters. Ostro and Pettengill (*2*), on the other hand, modeled the problem with surface craters and $N = 2$ only. For Europa and the example in Table 1, this would not be possible with the same active area unless the (FH/λ) term were increased from 10 to an unreasonably large value of 2200. Although other assumptions can ameliorate this result to some extent, it nevertheless supports Ostro's (*7*) conclusion that the requirement for very large coherent zones makes the surface-crater model an unlikely explanation for the observations. Figure 3 illustrates this point: clear acrylic hemispheres with faces up display the strong buried-crater response to incident radiation, whereas identical face-down hemispheres simulate one component of the return from surface craters.

Perhaps the feature of the observations that best permits discriminating between

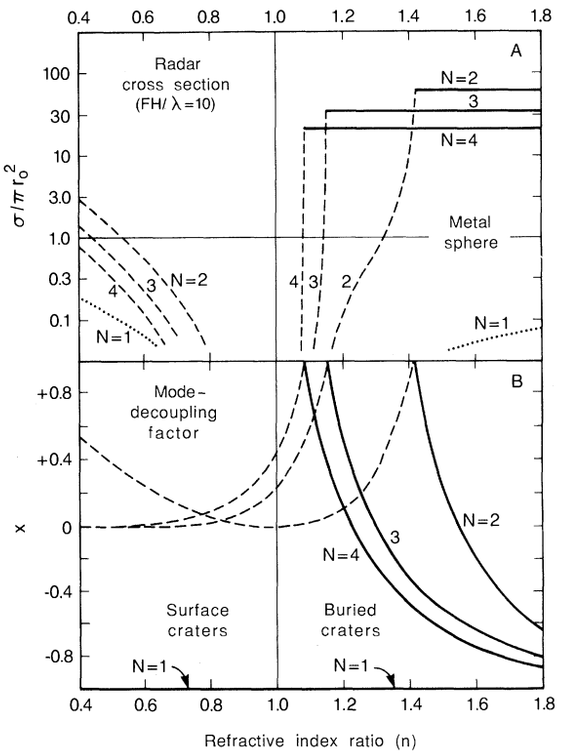

Fig. 2. (A) Normalized radar backscatter cross sections of surface and buried craters for $N = 1$ to 4 ray bounces. (B) The mode decoupling factor x of surface and buried craters for backscatter and $N = 1$ to 4 ray bounces. The heavy solid lines in both (A) and (B) indicate where total internal reflection occurs for $N \geq 2$.

models is the polarization distribution of the total echo energy (*1*). It has been shown (*5*) that the observed distributions (*7*) for all three moons can be explained by using a single numerical value for a mode decoupling factor, given by $x = 2e \cos\theta/(1 + e^2)$. For the craters being considered here, $e = (-\rho_{TM}/\rho_{TE})^N$; $\theta = 0$ when $n < n_c$ and $e = 1.0$;

$$\theta = 2N \tan^{-1}[(n_B/n)(n^2 - n_c^2)^{1/2}]$$

when $n > n_c$, where θ is the electrical phase difference between the TM and TE modes after they have bounced back out of the crater; and e involves the ratio of their amplitudes after N reflections. The value of x can range from -1 for simple reflection to $+1$ for pure refraction. Decoupling is due to differential mode amplitudes for surface craters, and to differential mode phases for buried craters when TIR occurs. The icy-moon echoes at $\lambda = 0.13$ m are well matched (*5*) by $x = 0.23$. Echoes from rocky planets and Earth's moon are compatible with $x \cong -0.8$.

The mode decoupling factor from the above expressions is plotted in Fig. 2B for $0.4 < n < 1.8$ (*8*). It is a very sensitive indicator of the detailed scattering mechanisms. With the requirement that $x = 0.23$, a value consistent with the observed polarizations, it follows that for each $N \geq 2$, there is one solution for n that involves TIR, and one or two additional solutions in the weak-echo regime depending on whether N is odd or even, respectively (*8*). The TIR solutions for $x = 0.23$ in Fig. 2B occur at $n = 1.51$ for $N = 2$, at $n = 1.26$ for $N = 3$, and at $n = 1.19$ for $N = 4$. For craters with $r_0 \cong 1$ to 10 m observed at nominal radar wavelengths, important echo contributions are not expected for $N \gtrsim 5$ because of a spillover effect for the coherent glints (*6*) plus the requirement for very steep crater walls for large N. Figure 2B shows that the value of $n = 1.225$ used in the example in Table 1 would produce $x = 0.23$ if there were approximately equal echo contributions from the $N = 3$ and 4 components. There is no direct information about the possible refractive discontinuities between resurfacing material and the original surface, but a ratio of this modest value would not be surprising. One might be less inclined to expect the larger n needed for TIR with $N = 2$. For example, if the overburden were ice at $n_3 = 1.78$, the TIR solution for $N = 2$ would require the refractive index of the base material, n_2, to be only 1.18, implying a density reduction by a factor of more than 4.

On the other hand, Saunders *et al.* (*9*) have exposed frozen mixtures of water and clay to a simulated space environment and found that sublimation of the ice can leave a structurally coherent residue of extremely low density. Surface frost deposits could also have very low densities. Thus the $N = 2$ solution appears to be a distinct possibility even if the resurfacing flood were to partially invade the voids of the frost or sublimation residue. For $N = 2$ and $FH/\lambda = 10$, $\sigma_2/\pi r_0^2 = 63$ when TIR occurs. In this case, only 4% of the surface area of Europa could produce its strong echoes whereas, if the $N = 3$ and 4 components also contributed, the coverage by buried craters could be as low as 2%.

It is important to emphasize that the crater base material need not be of low density throughout. There could be relatively pure ice almost everywhere except for a very thin layer, on the order of only a wavelength in thickness, where frost deposits or sublimation has reduced the density and refractive index as illustrated in Fig. 1C. This layer at the top of the old surface and its old crater walls would then provide the discontinuity for TIR in the subsequently flooded craters, while a developing low-density film near the top of the overburden would facilitate the passage of radar waves across the new upper surface.

The previous discussion is limited to the radar measurements that have been conducted at $\lambda = 0.13$ m. Observations have also been made of Ganymede at $\lambda = 0.035$ m and of Europa at $\lambda = 0.70$ m (*3, 7*). They indicate that the mode decoupling factor decreases with increasing λ, going from $x = 0.3$ at $\lambda = 0.035$ m to 0.23 at $\lambda = 0.13$ m and to approximately zero at $\lambda = 0.70$ m. In the TIR regime x is sensitive to small changes in the refractive discontinuity at the crater wall (Fig. 2B). The measured trend in x with λ would be expected if the refractive index discontinuity shown in Fig. 1B were not perfectly sharp but rather extended over the order of a decimeter in radius. That is, the evanescent waves in the base material would feel a larger discontinuity at longer wavelengths because they would extend slightly farther into this medium. The resulting increase in effective n would then cause a decrease in x as long as TIR occurs. For the above numbers and assuming $N = 3$ only, the effective n would be 1.24 at $\lambda = 0.035$ m, 1.26 at $\lambda = 0.13$ m, and about 1.30 at $\lambda = 0.70$ m. These small changes correspond to the observed large differences in echo polarizations. The thin n_2 layer of Fig. 1C would also produce this effect if it were graded and thick enough to exclude the longest wavelength evanescent waves from the deeper n_3 material.

The total echo strengths also depend upon λ as a result of several factors. The (FH/λ) term represents both an explicit inverse dependence of σ on λ and the expected effect of crater wall roughness in reducing the equivalent FH product at sufficiently short wavelengths. Also, absorption in most lossy materials increases with decreasing λ.

The principal support for the buried crater model is its success in explaining the strengths of the echoes, their unusual polarizations, and the observed radar brightness of the satellite limbs (*1*), all by a single kind of scattering center that could be created by processes that are known to occur. Modest additional support for craters as a source of the echoes is found in the correspondence between echo strengths and a theoretical prediction of relative cratering rates. In the

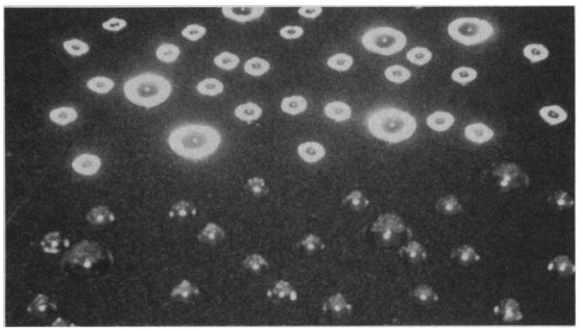

Fig. 3. Flash picture of acrylic cabochons of 1.3-cm and 2.5-cm diameter and nearly hemispherical shape simulates the strong radar response of buried craters (bright upturned faces) and one component of the weaker echoes from surface craters (faces down). The bright glory circles are not reflections from the flat faces (the angle of incidence is about $\pi/4$) but rather are due to total internal reflections.

Table 1. Normalized radar cross sections ($\sigma_N/\pi r_0^2$) for backscatter from surface and buried craters, under the conditions of Fig. 1, A and B, and other assumptions described in the text.

Bounces N	Surface crater $n = (0.5)^{1/2}$	Buried crater $n = (1.5)^{1/2}$	Buried/surface ratio
1	0.029	0.010	0.35
2	0.16	0.16	1.0
3	0.056	36	640
4	0.028	22	790
10	0.0038	3.9	1000
$N > 10$	$20(\pi/N)^2 \exp(-2\pi)$	$40(\pi/N)^2$	$2 \exp(2\pi)$

order Europa, Ganymede, and Callisto, $\sigma/\pi R^2$ at $\lambda = 0.13$ m is about 2.6, 1.5, and 0.6, whereas the cratering rates predicted by Shoemaker and Wolfe (*10*), when normalized to 2.6 for Europa, are 2.6, 1.3, and 0.7, respectively.

As used here, the descriptive term "buried craters" is meant to apply primarily to the electromagnetic model and only secondarily to the physical model. For example, in Fig. 1D, mechanical and thermal events during crater formation might compress or line the walls and produce a TIR source without the need for a later resurfacing flood. Craterlike geometry might also result from processes other than impacts; for example, differential freezing could create a source where the n_3 material of Fig. 1D fills the hemispheroidal n_2 void (*5*). This and the examples in Fig. 1, B, C, and D, all represent the electromagnetic model of buried craters. The most likely physical model is proposed here to be Fig. 1C.

Cratering and resurfacing have also occurred on rocky planets and Earth's moon. There are two reasons why the icy moons could display strong echoes from buried craters while the rocky bodies would not. The required TIR condition is plausible on icy moons but there is no comparable expectation for $n > 1$ interfaces on rocky bodies. Moreover, the loss coefficient for cold ice is much less than for the common minerals of the rocky surfaces, so that longer subsurface propagation paths are possible on the icy bodies.

There are three key requirements for further refinements in our understanding of the scattering process and its meaning in terms of the surface and subsurface characteristics of the three moons discussed here, and perhaps of dozens of other icy bodies in the outer solar system. First, the complete polarization properties of the echoes should be investigated by measuring either signal amplitudes at four polarizations or phase plus amplitude at two polarizations. Second, radar investigations using separated transmitters and receivers are needed to study scattering in other than the backward direction, and to determine how best to conduct radar mapping experiments. This could be done with powerful transmissions from Earth and reception at spacecraft near the targets (*11*). And finally, for all of the characteristics of the scattered radar signals there is a need for improved coverage and resolution so that detailed comparisons can be made with other sources of two-dimensional information, such as optical imaging.

REFERENCES AND NOTES

1. R. M. Goldstein and G. A. Morris, *Science* **188**, 1211 (1975); D. B. Campbell, J. F. Chandler, S. J. Ostro, G. H. Pettengill, I. I. Shapiro, *Icarus* **34**, 254 (1978); S. J. Ostro, D. B. Campbell, G. H. Pettengill, I. I. Shapiro, *ibid.* **44**, 431 (1980). Radar echoes from the icy moons are up to 2.6 times as strong as from perfectly reflecting metal spheres of the same size. Echoes from rocky planets and Earth's moon are roughly one-tenth the metal-sphere value. The polarization of waves reflected from rocky bodies is similar to that observed from large homogeneous spheres: incident waves polarized in the right-handed circular sense have echoes that are almost entirely polarized in the left-hand circular sense. Most of the energy in the echoes from the icy moons, however, is contained in the unexpected (right-handed in this case) circularly polarized component. Linearly polarized waves are also anomalously depolarized by the icy moons. For a homogeneous sphere, backscattered surface reflections come only from the center of the disk since off-normal incident rays are scattered in other directions. Although rocky-planet echoes are mainly from this central zone, the icy-moon echoes are strong from nearly all areas of the disk, so that, by comparison, the limbs appear to be unusually bright when observed by radar.
2. S. J. Ostro and G. H. Pettengill, *Icarus* **34**, 268 (1978).
3. R. M. Goldstein and R. R. Green, *Science* **207**, 179 (1980).
4. T. Hagfors, T. Gold, H. M. Ierkic, *Nature (London)* **315**, 637 (1985).
5. V. R. Eshleman, *ibid.* **319**, 755 (1986).
6. Radar cross section σ of a target is defined in such a way that $\sigma/\pi R^2 = 1$ for backscattering from a perfectly reflecting sphere of radius R large compared with the radar wavelength. For $N = 1$, $\sigma_1/\pi r_0^2 = (n-1)^2/(n+1)^2$. For $N \geq 2$, the glints have characteristic area $H\Delta r$ and radial width $\Delta r = (\lambda r_0 n_B/2n_c N)^{1/2}$. In the expression for σ_N, the magnitude of each ρ is unity for $n > n_c$, the condition for total internal reflection. The angle of incidence, measured between the ray direction and the normal to the crater wall at a reflection point, is nominally $(\pi/2)(1 - 1/N)$ so that $n_B = \tan(\pi/2N)$, $n_c = \sec(\pi/2N)$, and $n_c^2 = n_B^2 + 1$.
7. S. J. Ostro, in *Satellites of Jupiter*, D. Morrison, Ed. (Univ. of Arizona Press, Tucson, 1982), pp. 213–236.
8. For larger n, $x \rightarrow -1$ for all N. For smaller n and large N, x remains near zero until n is very close to zero, where it suddenly changes to $x = 1$ for even N and $x = -1$ for odd N at $n = 0$.
9. R. S. Saunders, T. J. Parkes, J. B. Stephens, E. G. Lane, F. P. Fanale, *Lunar Planet. Sci. Conf. Abstracts* **16**, 730 (1985).
10. E. M. Shoemaker and R. F. Wolfe, in *Satellites of Jupiter*, D. Morrison, Ed. (Univ. of Arizona Press, Tucson, 1982), pp. 277–339.
11. V. R. Eshleman *et al*, *Science* **223**, 772 (1984).

12. I thank G. L. Tyler, S. J. Ostro, R. A. Simpson, and T. Hagfors for helpful comments and discussion. Tyler had suggested an association of the radar observations with the glory even before the buried-crater model was devised. This work was supported by NASA.

12 May 1986; accepted 25 August 1986

Refractory Minerals in Interplanetary Dust

ROY CHRISTOFFERSEN* AND PETER R. BUSECK

A newly studied interplanetary dust particle contains a unique set of minerals that closely resembles assemblages in the refractory, calcium- and aluminum-rich inclusions in carbonaceous chondrite meteorites. The set of minerals includes diopside, magnesium-aluminum spinel, anorthite, perovskite, and fassaite. Only fassaite has previously been identified in interplanetary dust particles. Diopside and spinel occur in complex symplectic intergrowths that may have formed by a reaction between condensed melilite and the solar nebula gas. The particle represents a new link between interplanetary dust particles and carbonaceous chondrites; however, the compositions of its two most abundant refractory phases, diopside and spinel, differ in detail from corresponding minerals in calcium- and aluminum-rich inclusions.

INTERPLANETARY DUST PARTICLES (IDP's) and carbonaceous chondrite meteorites are two types of extraterrestrial materials known to contain unprocessed components of the early solar system. IDP's of the chondritic subgroup chemically resemble carbonaceous chondrites (*1*) and contain some of the same principal minerals (*2, 3*). However, they exhibit enough textural and detailed mineralogical differences from carbonaceous chondrites to leave unanswered many questions regarding the relative formation histories of the two materials.

An unresolved aspect of the relation between IDP's and carbonaceous chondrites concerns the differences in their so-called refractory minerals, that is, the phases considered to be the highest temperature products of the solar nebula (*4*). Unusual enstatite crystals within some IDP's show evidence of being high-temperature nebular condensates (*5*). This finding raised the expectation that some IDP's might also contain samples of the more refractory, calcium- and aluminum-rich phases predicted to form in the solar nebula (*4*). Such refractory nebular materials occur in calcium- and aluminum-rich inclusions (CAI's) from certain carbonaceous chondrites, meteorites in which the mineralogy, chemistry, and isotopic composition of CAI's have been studied intensely (*6*). To our knowledge, however, the identification of fassaite in one IDP sample (*7*) has been the only instance where a phase characteristic of CAI's has been found in a chondritic IDP, and refractory phases have largely remained the "missing links" of IDP mineralogy.

We report transmission electron micro-

Departments of Geology and Chemistry, Arizona State University, Tempe, AZ 85287.

*Present address: Department of Geology, Indiana University, Bloomington, IN 47405.